Published in final edited form as:
J Magn Reson. 2013 December ; 237: 169–174. doi:10.1016/j.jmr.2013.10.013.

Low-field MRI can be more sensitive than high-field MRI

Aaron M. Coffey[1,2], **Milton Truong**[1], and **Eduard Y. Chekmenev**[1,2,3]

[1]Department of Radiology, Vanderbilt University Institute of Imaging Science (VUIIS), Nashville, Tennessee, 37232, United States

[2]Department of Biomedical Engineering, Vanderbilt University, Nashville, Tennessee, 37235, United States

[3]Department of Biochemistry, Vanderbilt University, Nashville, Tennessee, 37205, United States

Abstract

MRI signal-to-noise ratio (SNR) is the key factor for image quality. Conventionally, SNR is proportional to nuclear spin polarization, which scales linearly with magnetic field strength. Yet ever-stronger magnets present numerous technical and financial limitations. Low-field MRI can mitigate these constraints with equivalent SNR from non-equilibrium 'hyperpolarization' schemes, which increase polarization by orders of magnitude independently of the magnetic field. Here, theory and experimental validation demonstrate that combination of field independent polarization (*e.g.* hyperpolarization) with frequency optimized MRI detection coils (i.e. multi-turn coils using the maximum allowed conductor length) results in low-field MRI sensitivity approaching and even rivaling that of high-field MRI. Four read-out frequencies were tested using samples with identical numbers of ^{1}H and ^{13}C spins. Experimental SNRs at 0.0475 T were ∼40% of those obtained at 4.7 T. Conservatively, theoretical SNRs at 0.0475 T 1.13-fold *higher* than 4.7 T were possible despite an ∼100-fold lower detection frequency, indicating feasibility of high-sensitivity MRI without technically challenging, expensive high-field magnets. The data at 4.7 T and 0.0475 T was obtained from different spectrometers with different RF probes. The SNR comparison between the two field strengths accounted for many differences in parameters such as system noise figures and variations in the probe detection coils including *Q* factors and coil diameters.

Keywords

hyperpolarization; MRI; NMR; low-field MRI; Litz wire; 13C

1. Introduction

The superlative factor governing MRI image quality is the signal-to-noise ratio (SNR). High-field MRI using superconductive magnets has revolutionized medical diagnostics, with ever-increasing magnetic fields fostering sensitivity improvements via higher SNR. Yet low magnetic field strengths offer many attractive advantages such as reduced magnet size and cost, greater subject safety due to lower absorption of radio-frequency energy, and

Correspondence to: Eduard Y. Chekmenev.

negligible subject induced magnetic field inhomogeneities [1]. These low-field MRI advantages can potentially be truly transformative, permitting performance of the entire MRI exam in seconds [2] provided sufficient SNR is available. The SNR of conventional, higher field detection is a complex equation of nuclear spin polarization, detection frequency, and other factors [3] arising from Faraday inductive detection. Nuclear spin polarization is a key factor contributing to this SNR. It is a relative measure of nuclear spin alignment with the applied magnetic field B_0. Equilibrium nuclear spin polarization, which is only 10^{-6} -10^{-5} at conditions of human body temperature and B_0 of several Tesla, scales linearly with B_0 and, therefore, SNR decreases at low field. However, non-equilibrium 'hyperpolarization' schemes make polarization independent of the detection field, providing a unique opportunity for high SNR and image quality at low field.

Hyperpolarization techniques temporarily increase polarization by several orders of magnitude to unity, or 10^0, referred to as the hyperpolarized state. These techniques include dissolution-Dynamic Nuclear Polarization (DNP) [4], Para-Hydrogen and Synthesis Allow Dramatically Enhanced Nuclear Alignment (PASADENA) [5], Spin Exchange Optical Pumping (SEOP) [6] and others. Regardless of the hyperpolarization approach used, the main goal in the context of biomedical applications is preparation of exogenous contrast agents with high polarization to enable molecular imaging of relatively dilute spin systems otherwise not amenable by conventional MRI. Examples of such contrast agents include hyperpolarized noble gases for lung imaging and ^{13}C-labeled metabolites. The latter can be out of balance due to abnormal metabolism, and therefore act as reporters or biomarkers of diseases including those of cancer. ^{13}C-pyruvate contrast agent reporting on elevated rate of glycolysis in cancer is one such example already in clinical trial [7] due to recognized status as a promising molecular imaging agent for prostate cancer.

While low-field MRI has been shown useful for hyperpolarized states of noble gases in lung imaging [8] and much progress has been made for utilizing hyperpolarized contrast agents in molecular imaging [4, 7], the B_0 field independent nature of polarization in hyperpolarized contrast agents has not been fully taken advantage of. Maximizing imaging detection sensitivity as a function of both detection field B_0 [9] and frequency ω_0 still remains a challenge. Prior systematic efforts to develop a theoretical SNR foundation for MRI neglected optimization of the Faraday induction coils to the detection frequency ω_0 [3, 9-11]. We recently demonstrated ^{13}C hyperpolarized signals can be nearly field independent [12]. Here, we present a general theoretical description of *hyperpolarized* MRI sensitivity in the form of SNR as a function of detection frequency ω_0 and experimental validation at four frequencies: 0.5 MHz, 2.0 MHz, 50 MHz, and 200 MHz. It is concluded that low-field MRI can be significantly more sensitive than high-field MRI for detection of hyperpolarized spin states. This is contrary to conventional wisdom that high-field MRI is always more sensitive.

2. Materials and Methods

Sample phantoms and preparation of nuclear spin polarizations

^{1}H and ^{13}C spectroscopic and imaging comparisons utilized two spherical phantoms of sodium 1-^{13}C-acetate. The phantom for ^{1}H studies was 1.0 g of sodium 1-^{13}C-acetate (product #279293, Isotec-Sigma-Aldrich) dissolved in 99.8% D_2O resulting in 2.8 mL total volume. A larger sample for ^{13}C studies consisted of 5.18 g of sodium 1-^{13}C-acetate dissolved in 99.8% D_2O resulting in 17.5 mL total volume. High-field data were acquired on a 4.7 T Varian small animal MRI scanner with a multi-nuclear RF probe (Doty Scientific, Columbia, SC). Low-field data were collected on a 0.0475 T spectrometer (Magritek, Wellington, New Zealand) equipped with a custom gradient coil insert (Magritek) and in-house developed H-X and X-H radiofrequency (RF) probes, where the X channel was tuned and optimized to the ^{13}C resonance frequency. The in-house probes consisted of inner ω_0

optimized solenoid detection coils and outer saddle excitation coils for multi-nuclear experiments. The details are provided in Supporting Information.

Prior to spectroscopic or MR imaging at 0.0475 T as shown in Figs. 1 and 2, the sample was prepolarized [13]. Prepolarization for detection at 0.0475 T was necessary to (i) simulate the condition of the hyperpolarized state (when nuclear spin polarization significantly exceeds the Boltzmann distribution), and (ii) to obtain nuclear spin polarization close to 4.7 T Boltzmann equilibrium levels for comparison of detected SNR. For ^{1}H studies, the sample was prepolarized at 9.4 T for > 30 seconds, and detection at 0.0475 T occurred following an ∼5 second transfer delay. At detection, the resulting ^{1}H polarization was $P = (1.050\pm0.016)*10^{-5}$. Polarization level was calculated by comparison of the prepolarized NMR signal intensity with that of the thermally polarized sample. Conditions simulating hyperpolarized ^{1}H detection were explored in addition to ^{13}C detection because of the potential advantages of indirect proton MRI of hyperpolarized contrast agents *in vivo* [14]. Similarly for ^{13}C studies, the sample was prepolarized at 7.0 T for > 5 minutes, and detected at 0.0475 T following an ∼5 second transfer delay. ^{13}C polarization was calculated as $P = (4.70\pm0.02)*10^{-6}$ by comparing prepolarized NMR signal intensity with that of the thermally polarized sample.

Spectroscopic results (Fig. 2) used identical acquisition parameters on the two MRI systems: square RF excitation pulses with calibrated $\tau_{90°}$, 1 k complex acquisition points, spectral width of 2 kHz, and 500 ms acquisition time. Imaging (Fig. 1) was similarly performed with identical parameters with the exception of ^{13}C RF excitation pulse angle α. On the 4.7 T scanner, images were acquired with Varian's 2D balanced FSSFP sequence. At 0.0475 T, Magritek's fast 2D gradient echo sequence was used. For ^{1}H on both systems RF excitation pulse angle $\alpha = 18°$, spectral width was 10 kHz, and acquisition time was 6.4 ms per line of k-space. ^{13}C imaging parameters were spectral width of 5 kHz, 6.4 ms acquisition time, pulse angle $\alpha = 90°$ at 4.7 T, and $\alpha = 18°$ at 0.0475 T. For the latter the reduced angle was necessary to avoid consuming too much polarization during gradient echo imaging acquisition of k-space. ^{1}H imaging in-plane resolution was 0.375×0.375 mm^2, (field of view = 24×24 mm^2), and ^{13}C was 2.5×2.5 mm^2 (field of view = 80×80 mm^2) respectively. The resulting ^{1}H and ^{13}C images had 64×64 and 32×32 imaging matrices, and they are presented without any extrapolation or any further manipulation.

3. Results and Discussion

Seminal work by Hoult [3, 15] described the SNR for Faraday inductive detection of the MRI signal in RF coils as

$$\Psi_{rms} = \frac{1}{\sqrt{2}}\frac{|\varepsilon|}{V} = \frac{KB_1V_S\omega_0\mu_N PN}{\sqrt{2}[4Fk\Delta f(T_C\zeta R_C + T_S R_S)]^{1/2}}. \quad (1)$$

Eq. (1) relates the magnitude of the electromotive force induced in the RF coil $|\varepsilon|$, noise V, oscillating RF field homogeneity over the subject K, oscillating RF field strength per unit current over the subject B_1, subject volume V_S, detection frequency ω_0, nuclear magnetic moment μ_N, nuclear spin polarization P, number of spins N, preamplifier noise figure F, Boltzmann's constant k, receiver bandwidth Δf, RF coil temperature T_C, proximity effect factor ζ, RF coil resistance R_C, subject temperature T_S, and equivalent subject resistance $R_S = R_I + R_E$, the sum of subject inductive and dielectric losses respectively [16, 17], also known as body noise. With the RF coil of a fixed geometry (*e.g.* same wire length, number of turns, etc.), polarization P induced by B_0, and negligible body noise from the subject with respect to RF coil noise (i.e. conditions of $T_C\zeta R_C \gg T_S R_S$), then by Eq. (1) for a range of

detection frequencies the $SNR \propto \omega_0^{7/4}$, corresponding to the common situation of high resolution NMR [18].

However, if the polarization is endowed by hyperpolarization produced independently of the detection magnetic field, the $SNR \propto \omega_0^{7/4}$ dependence becomes $SNR \propto \omega_0^{3/4}$, because one ω_0 is eliminated. Additionally, if the RF detection coil is optimized by using a maximum conductor length l consonant with ω_0 of up to $\lambda/10$ to create turns (i.e. forming multi-turn inductors while avoiding challenges such as onset of elevated electromagnetic radiation losses owing to increasing efficiency as antennas) [19], then SNR dependence on detection frequency ω_0 becomes more complex to evaluate. The rule $l = \lambda/10$ for maximum, continuous conductor length finds alternative expression in terms of the detection frequency ω_0 as $l = \pi ac/5\omega_0$, where ac is the conductor's wave propagation velocity. Provided the coil diameter d_C is fixed, lowering ω_0 then results in greater conductor length l and hence more turns n, variables common to both B_1 and R_C. Thus, the resonance frequency defines the number of turns n and the conductor length l using this approach. This commonality represents an underlying frequency dependency which may be consolidated; see Appendix A. for details pertaining to modification of Eq. (1) using $l = \pi ac / 5\omega_0$ to redefine B_1 and R_C in terms of the resonance frequency. With B_1 and R_C in Eq. (1) expressed as consolidated functions of ω_0, then for the condition of coil noise dominance, or $T_C\zeta R_C \gg T_S R_S$, SNR for the hyperpolarized state becomes

$$\Psi_{rms,hp} = \frac{1}{\sqrt{5}\cdot 2^{5/4}} \frac{KV_S \mu_N PN}{[\mu_r \rho (T_C)]^{1/4}} \left(\frac{\alpha c d_W}{FkT_C \Delta f \zeta} \right)^{1/2} \frac{\mu_0^{3/4} \omega_0^{1/4}}{d_C^2} \quad (2)$$

for wire diameter d_W, coil diameter d_C, permeability of free space μ_0, relative conductor permeability μ_r, conductor resistivity ρ, and velocity factor α correcting the speed of light c to conductor wave propagation velocity. Eq. (2) states SNR is a function of coil geometry, basic conductor properties, and fundamental physical constants. It can be recast to the condition of non-hyperpolarized (i.e. thermal) polarization for ω_0 optimized RF coils by substituting polarization induced by B_0 into Eq. (2), *or* $P = const \cdot \omega_0$ (see Appendix A). Consequently, Eq. (2)'s $\omega_0^{1/4}$ dependence becomes $\omega_0^{5/4}$. The $\omega_0^{5/4}$ dependence differs from conventional $\omega_0^{7/4}$ dependence [3] owing to an additional cancellation factor of $\omega_0^{1/2}$ obtained from interplay of gains and losses associated with the terms B_1 and R_C under the condition of $l = \lambda/10 = \pi ac / 5\omega_0$. While $\omega_0^{5/4}$ dependence clearly retains the favorability of conventional MR detection at higher fields, $SNR \propto \omega_0^{1/4}$ For hyperpolarized spin states produced independently of the detection magnetic field represents very weak frequency dependence.

As $SNR \propto \sqrt{Q}$ [3, 11] low-field detection may offer a favorable arena for SNR improvements on the basis of Q. The inductor electrical quality factor Q is expressed as $Q = \omega_0 L / R_C$, where L and R_C are the coil inductance and resistance respectively. While $Q \propto \omega_0^{1/2}$ for $T_C\zeta R_C \gg T_S R_S$ conventionally [20] (i.e. sample losses are negligible), the frequency optimized coil (where $l = \pi ac / 5\omega_0$) has a more complex dependence of Q on frequency ω_0 because $Q \propto \omega_0^{1/2} L$ and L itself exhibits frequency dependence due to change in the number of turns and other coil geometric factors. Nevertheless, a detailed analysis of experimental Q values is provided in the Supporting Information. To summarize, the Q values of the tuned RF circuits were 28 (0.5 MHz), 90 (50 MHz), 62 (2.0 MHz), 69 (200 MHz).

As illustrated by Eq. (2), low-field MRI affords unique opportunities to significantly increase overall SNR when RF coil noise dominates for detection frequencies below 10 MHz [15], or $T_C\zeta R_C \gg T_S R_S$. Low-field magnets allow solenoid geometry for the RF detection coil [8], unlike the high field's volume coils— birdcage, Alderman-Grant, and others— which permits 2.6-fold more efficient use of wire to form inductive loops resulting in 3.1-fold greater overall SNR [3]. 100-fold frequency differences result in only 3.2-fold SNR difference. Thus, coil geometry alone nearly compensates a 100-fold decrease in detection frequency for hyperpolarized spin states, 3.1 versus 3.2. Other wire-related factors present opportunities for further SNR gains.

Low field affords SNR challenges and opportunities related to the RF coil conductor. The proximity effect ζ between neighboring turns in multi-turn RF coils increases resistance R_C with concomitant SNR loss. However, this loss can be minimized through unique winding geometries as exemplified by crystal radio coils where improved turn density and hence B_1 promote higher SNR. Coil resistance R_C can simply be directly minimized for higher SNR through lowering coil temperature T_C and using Litz wire [21] or superconducting wire. Albeit constructing superconducting or reduced temperature T_C RF detection coils is a technological feat, using Litz wire is straightforward. Coil resistance reduction by a practical Litz wire factor of 0.44 due to reduced ζ and skin effect losses [21], for example, leads to SNR gain by 1.5 fold. Consequently, low-field SNR for hyperpolarized states better than high-field SNR is possible despite ζ loss related challenges on the order of 1.3 for RF coils with equally spaced wire and a length-to-diameter ratio of two [22]. We note that Litz wire does not provide benefits at the frequencies of high-field MRI coils. Nevertheless, MR detection at 100-fold lower frequency should yield 1.13-fold greater SNR compared to high-frequency detection (details given in Supporting Information, Table S6).

The estimated 1.13-fold SNR gain is very conservative. The afore-mentioned superconducting low-field RF coils can provide further SNR gains of as much as an order of magnitude [20]. Additionally, the hyperpolarized state's $SNR \propto \omega_0^{1/4}$ stems from using lossy conductors ($R_C \neq 0$) with frequency dependent resistance, whereas superconducting RF coils ($R_C = 0$) have SNR nominally independent of detection frequency ω_0, ignoring subject losses R_S [9]. Subject losses are negligible in the low-frequency regime for clinical scale RF coils [1], but clinical high-field MRI at $B_0 \geq 1.5$ T is well known for body noise being greater than coil noise, i.e. $T_S R_S \gg T_C \zeta R_C$ [20]. Also, while dielectric losses R_E are commonly mitigated by various techniques, subject inductive losses $R_I \propto \omega_0^2$ [3, 11, 15, 23-26] are inescapable. Thus, subject noise limits the overall SNR achievable at both high field and low field, but proves more favorable at lower frequencies. We note that not fulfilling the condition of coil noise dominance, or $T_C\zeta R_C \gg T_S R_S$, invalidates Eq. (2), but fully accounting for R_S in the context of ω_0 optimized coils is very complex and outside the main scope of this work. It should be stressed, however, that fundamental subject noise barriers hinder high-field detection [15] of hyperpolarized contrast agents.

Experimental validation of Eq. (2) analyzed ^{1}H and ^{13}C SNR for similar ^{1}H and ^{13}C spin polarization P of identical samples on 4.7 T Varian and 0.0475 T MRI scanners. Figs. 1 and 2 demonstrate imaging and spectroscopic detection using frequency optimized RF coils with similar coil sizes suitable for *in vivo* animal studies. After accounting for experimental limitations and imperfections when working with two different MRI systems (Supporting Information, Table S4), then by Eq. (2) the theoretical ratio of SNRs at 0.0475 T and 4.7 T magnetic field strengths (i.e. $SNRs_{0.0475T}/SNR_{4.7T}$) was 45% for ^{1}H and 46% for ^{13}C respectively. Using spectroscopic acquisition, Fig. 2, the experimentally determined ratio of SNRs at 0.0475 T and 4.7 T was 41±1% for ^{1}H and 40±1% for ^{13}C. This reflects good quantitative agreement with theory despite nearly 100-fold difference in field and frequency. While $SNR_{0.0475T}/SNR_{4.7T}$ of 113% was expected theoretically for detection of ^{1}H and ^{13}C

nuclei, experimental limitations as described in the Supporting Information significantly hampered ^{1}H and ^{13}C detection sensitivity at 0.0475 T. In particular, deviation from ideal Litz wire selection and RF coil coupling to other components due to a severe space limitation of an 89-mm I.D. gradient insert bore reduced achievable maximum SNR by a factor of 2.

The presented work is motivated by low-field MRI of ^{13}C hyperpolarized contrast agents through direct detection or indirectly through protons. Proton detection takes advantage of long-lived hyperpolarization stored on ^{13}C carboxyl carbons with the added benefits of increased sensitivity and lower gradient power requirements [7] *in vitro* [27] and *in vivo* [14]. The above theoretical and experimental SNR comparison of low and high field detection was conducted under the condition of RF coil noise dominance rather than subject/body noise dominance. The latter is in fact typical for high-field MRI of large animals and humans [20]. Subject noise disproportionately penalizes high field [20] but not low-field inductive detection [1]. As a result, this framework of RF coil optimization through maximized use of conductor length (i.e. approaching $l = \lambda/10 = \pi ac / 5\omega_0$) will likely favor hyperpolarized contrast agent low-field detection at clinical scale even more.

4. Conclusion

To summarize, a theoretical basis for SNR of hyperpolarized contrast agents as a function of detection frequency is described and validated experimentally. Low-field MRI can indeed be more sensitive for hyperpolarized contrast agents. Moreover, hyperpolarized low-field MRI in combination with cryogenically cooled RF coils [20, 28] can significantly surpass the sensitivity of hyperpolarized high-field MRI, which contradicts the 'conventional wisdom' of high-field MRI SNR superiority. In conclusion, low-field hyperpolarized MRI has the potential to revolutionize molecular imaging by providing better quality images, allowing sub-minute examinations at a significantly reduced cost, and perhaps solving one of the greatest challenges in Radiology: advancing human health while reducing the costs [29] of emerging great technologies [30].

Supplementary Material

Refer to Web version on PubMed Central for supplementary material.

Acknowledgments

We thank Professor Boyd M. Goodson for his comments on the writing of the manuscript and gratefully acknowledge funding support from NIH R25 CA136440, 3R00 CA134749, DOD CDMRP W81XWH-12-1-0159/BC112431.

Appendix A. Derivations of SNR equations

The SNR for MRI has been described in seminal work by Hoult [3, 15] for Faraday inductive detection of the MRI signal in radiofrequency (RF) coils as

$$\Psi_{rms} = \frac{1}{\sqrt{2}}\frac{|\varepsilon|}{V} = \frac{KB_1V_S\omega_0\mu_N PN}{\sqrt{2}[4Fk\Delta f(T_C\zeta R_C + T_S R_S)]^{1/2}} \quad \text{(A1)}$$

where the equation variables are as previously defined for Eq. (1). With the RF coil of a fixed geometry— e.g. same wire length, number of turns, etc.— polarization P induced by B_0, and negligible sample noise with respect to RF coil noise, i.e. conditions of $T_C\zeta R_C \gg T_S R_S$, then by Eq. (A1) the $SNR \propto \omega_0^{7/4}$. However, if polarization P is endowed by

hyperpolarization independent of B_0 and the RF detection coil is specifically optimized for ω_0, i.e. using the maximum allowed conductor length or using $l = \lambda/10$, SNR dependence on detection frequency ω_0 becomes more complex due to B_1 and R_C frequency dependency.

An optimal RF coil's maximum allowed conductor length is $l = \lambda/10$ when maintaining current phase across the coil. The detection frequency ω_0 explicitly defines this length in lieu of wavelength λ, since $\alpha c = (\lambda\omega_0)/(2\pi)$, as

$$l=\frac{\pi\alpha c}{5\omega_0}. \quad \text{(A2)}$$

Velocity factor α corrects the speed of light c to the conductor's wave propagation velocity. The RF field B_1 generated by conductor unit current J finds similar re-expression. In the quasi-static limit Biot-Savart law defines B_1 [3] generated by n loops of radius a as [31]

$$\frac{B_1(z)}{J}=\frac{\mu_0 n}{2}\frac{a^2}{(z^2+a^2)^{3/2}} \quad \text{(A3)}$$

for distance z from the RF coil center and permeability of free space μ_0. Albeit direct calculation of B_1 homogeneity factor K is feasible [32], since $K \sim 1$ typically and coil diameter $d_C = 2a$, B_1 over the sample is approximately B_1 at the coil center ($z = 0$), or

$$\frac{B_1(0)}{J}=\mu_0\left(\frac{n}{d_C}\right). \quad \text{(A4)}$$

With coil length $l_C \ll l$ for $n > 1$, $n = (l - l_C)/\pi d_C \approx l/\pi d_C$ and B_1 is written as

$$B_1=\frac{\mu_0\alpha c}{5\omega_0 d_c^2}. \quad \text{(A5)}$$

The inverse proportionality in B_1 with respect to ω_0 in Eq. (A5) is driven by the change in the number of turns n, Eq. (A4) under the condition of fixed coil diameter d_C and the condition imposed by Eq. (A2).

The current J reduces exponentially to 1/e of its conductor surface value at a distance known as the skin depth δ, which varies with ω_0 as

$$\delta=\left(\frac{2\rho(T_C)}{\mu_r\mu_0\omega_0}\right)^{1/2} \quad \text{(A6)}$$

for relative permeability μ_r and temperature dependent resistivity ρ. J flows through an effective cross-sectional areal product of δ and conductor circumference, or $A = \pi d_W\delta$, for wire diameter d_W. When constructed of a single, solid conductor, coil resistance R_C is expressed using Eq. (A2) and Eq. (A6) as

$$R_c=\frac{\rho l}{A}=\frac{\rho l}{\pi d_W\delta}=\left(\frac{\alpha c}{5d_W}\right)\left(\frac{\mu_r\mu_0\rho(T_C)}{2\omega_0}\right)^{1/2}. \quad \text{(A7)}$$

When Eqs. (A5) and (A7) are substituted into Eq. (A1), Eq. (A1) becomes for conditions $T_C\zeta R_C \gg T_S R_S$

$$\Psi_{rms,hp}=\frac{1}{\sqrt{5}\cdot 2^{5/4}}\frac{KV_S\mu_N PN}{[\mu_r\rho(T_C)]^{1/4}}\left(\frac{\alpha c d_W}{FkT_C\Delta f\zeta}\right)^{1/2}\frac{\mu_0^{3/4}\omega_0^{1/4}}{d_C^2}. \quad \text{(A8)}$$

The proportionality to detection frequency of $\omega_0^{1/4}$ Stems from using lossy conductors, Eq. (A7).

With polarization P endowed by B_0, i.e. the non-hyperpolarized condition, polarization is written as

$$P=\frac{\hbar(I+1)\omega_0}{3kT_S}. \quad \text{(A9)}$$

After substitution of Eq. (A9) and nuclear magnetic moment $\mu_N \equiv \gamma\hbar I$, Eq. (A8) becomes

$$\Psi_{rms}=\frac{1}{3\sqrt{5}\cdot 2^{5/4}}\frac{KV_S\gamma\hbar^2 I(I+1)N}{kT_S[\mu_r\rho(T_C)]^{1/4}}\left(\frac{\alpha c d_W}{FkT_C\Delta f\zeta}\right)^{1/2}\frac{\mu_0^{3/4}\omega_0^{5/4}}{d_C^2} \quad \text{(A10)}$$

for gyromagnetic ratio γ, Planck's constant $\hbar$, and nuclear spin number I.

References

1. Hayden ME, Bidinosti CP, Chapple EM. Specific absorption rates and signal-to-noise ratio limitations for MRI in very-low magnetic fields. Concept Magnetic Res A. 2012; 40A:281–294.
2. Imai H, Kimura A, Hori Y, Iguchi S, Kitao T, Okubo E, Ito T, Matsuzaki T, Fujiwara H. Hyperpolarized ^{129}Xe lung MRI in spontaneously breathing mice with respiratory gated fast imaging and its application to pulmonary functional imaging. NMR Biomed. 2011; 24:1343–1352. [PubMed: 21538635]
3. Hoult DI, Richards RE. The signal-to-noise ratio of the nuclear magnetic resonance experiment. J Magn Reson. 1976; 24:71–85.
4. Golman K, in't Zandt R, Thaning M. Real-time metabolic imaging. Proc Natl Acad Sci U S A. 2006; 103:11270–11275. [PubMed: 16837573]
5. Bowers CR, Weitekamp DP. Para-Hydrogen and Synthesis Allow Dramatically Enhanced Nuclear Alignment. J Am Chem Soc. 1987; 109:5541–5542.
6. Walker TG, Happer W. Spin-exchange optical pumping of noble-gas nuclei. Rev Mod Phys. 1997; 69:629–642.
7. Kurhanewicz J, Vigneron DB, Brindle K, Chekmenev EY, Comment A, Cunningham CH, DeBerardinis RJ, Green GG, Leach MO, Rajan SS, Rizi RR, Ross BD, Warren WS, Malloy CR. Analysis of Cancer Metabolism by Imaging Hyperpolarized Nuclei: Prospects for Translation to Clinical Research Neoplasia. 2011; 13:81–97.
8. Tsai LL, Mair RW, Rosen MS, Patz S, Walsworth RL. An open-access, very-low-field MRI system for posture-dependent He-3 human lung imaging. J Magn Reson. 2008; 193:274–285. [PubMed: 18550402]
9. Myers W, Slichter D, Hatridge M, Busch S, Mössle M, McDermott R, Trabesinger A, Clarke J. Calculated signal-to-noise ratio of MRI detected with SQUIDs and Faraday detectors in fields from 10μT to 1.5T. J Magn Reson. 2007; 186:182–192. [PubMed: 17337220]

10. Carias MF, Dominguez-Viqueira W, Santyr GE. Improving Signal-to-Noise Ratio of Hyperpolarized Noble Gas MR Imaging at 73.5 mT Using Multiturn Litz Wire Radiofrequency Receive Coils. Concept Magnetic Res B. 2011; 39B:37–42.
11. Dominguez-Viqueira W, Berger W, Parra-Robles J, Santyr GE. Litz Wire Radiofrequency Receive Coils for Hyperpolarized Noble Gas MR Imaging of Rodent Lungs at 73.5 mT. Concept Magnetic Res B. 2010; 37B:75–85.
12. Coffey AM, Shchepin RV, Wilkens K, Waddell KW, Chekmenev EY. A Large Volume Double Channel ^{1}H-X RF Probe for Hyperpolarized Magnetic Resonance at 0.0475 Tesla. J Magn Reson. 2012; 220:94–101. [PubMed: 22706029]
13. Pound RV. Nuclear Spin Relaxation Times in Single Crystals of LiF. Physical Review. 1951; 81:156–156.
14. Mishkovsky M, Cheng T, Comment A, Gruetter R. Localized in vivo hyperpolarization transfer sequences. Magn Reson Med. 2012; 68:349–352. [PubMed: 22190079]
15. Hoult DI, Lauterbur PC. The sensitivity of the zeumatographic experiment involving human samples. J Magn Reson. 1979; 34:425–433.
16. Gadian DG, Robinson FNH. Radiofrequency losses in NMR experiments on electrically conducting samples. J Magn Reson. 1979; 34:449–455.
17. Redpath TW, Hutchison JMS. Estimating patient dielectric losses in NMR images. Magn Reson Imaging. 1984; 2:295–300. [PubMed: 6530932]
18. Minard KR, Wind RA. Solenoidal microcoil design - Part II: Optimizing winding parameters for maximum signal-to-noise performance. Concept Magnetic Res. 2001; 13:190–210.
19. Terman FE. Radio Engineers's Handbook. 1943
20. Darrasse L, Ginefri JC. Perspectives with cryogenic RF probes in biomedical MRI. Biochimie. 2003; 85:915–937. [PubMed: 14652180]
21. Lotfi, AW.; Lee, FC. A high frequency model for Litz wire for switch-mode magnetics. Industry Applications Society Annual Meeting, Conference Record of the 1993 IEEE; 1993. p. 1169-1175.
22. Medhurst RG. H. F. Resistance and Self-Capacitance of Single-Layer Solenoids. Wireless Engineer. Feb.1947 Mar.:35–43. 80-92.
23. Marrocco BJD, Drost DJ, Prato FS. An optimized head coil design for MR imaging at 0.15-T. Magn Reson Med. 1987; 5:143–159. [PubMed: 3657503]
24. Bidinosti CP, Chapple EM, Hayden ME. The sphere in a uniform RF field - Revisited. Concept Magnetic Res B. 2007; 31B:191–202.
25. Gilbert KM, Scholl TJ, Chronik BA. RF coil loading measurements between 1 and 50 MHz to guide field-cycled MRI system design. Concept Magnetic Res B. 2008; 33B:177–191.
26. Blasiak B, Volotovskyy V, Deng C, Tomanek B. An optimized solenoidal head radiofrequency coil for low-field magnetic resonance imaging. Magn Reson Imaging. 2009; 27:1302–1308. [PubMed: 19559554]
27. Chekmenev EY, Norton VA, Weitekamp DP, Bhattacharya P. Hyperpolarized ^{1}H NMR Employing Low gamma Nucleus for Spin Polarization Storage. J Am Chem Soc. 2009; 131:3164–3165. [PubMed: 19256566]
28. Resmer F, Seton HC, Hutchison JMS. Cryogenic receive coil and low noise preamplifier for MRI at 0.01 T. J Magn Reson. 2010; 203:57–65. [PubMed: 20031458]
29. Matlashov AN, Schultz LJ, Espy MA, Kraus RH, Savukov IM, Volegov PL, Wurden CJ. SQUIDs vs. Induction Coils for Ultra-Low Field Nuclear Magnetic Resonance: Experimental and Simulation Comparison. IEEE Transactions on Appiled Superconductivity. 2011; 21:465–468.
30. Lee VS. MRI: From science to society. J Magn Reson Imaging. 2013; 37:753–760. [PubMed: 23441004]
31. Jin J. Electromagnetic analysis and design in magnetic resonance imaging. CRC PressI Llc. 1999
32. Minard KR, Wind RA. Solenoidal micro coil design. Part I: Optimizing RF homogeneity and coil dimensions. Concept Magnetic Res. 2001; 13:128–142.

Highlights

- SNR theory of hyperpolarized MR as a function of B_0 and frequency optimized RF coil
- Low-field MRI sensitivity approaches and even rivals that of high-field MRI
- RF coil development for low-field MR
- Multi-nuclear imaging and spectroscopy of hyperpolarization at low B_0 field

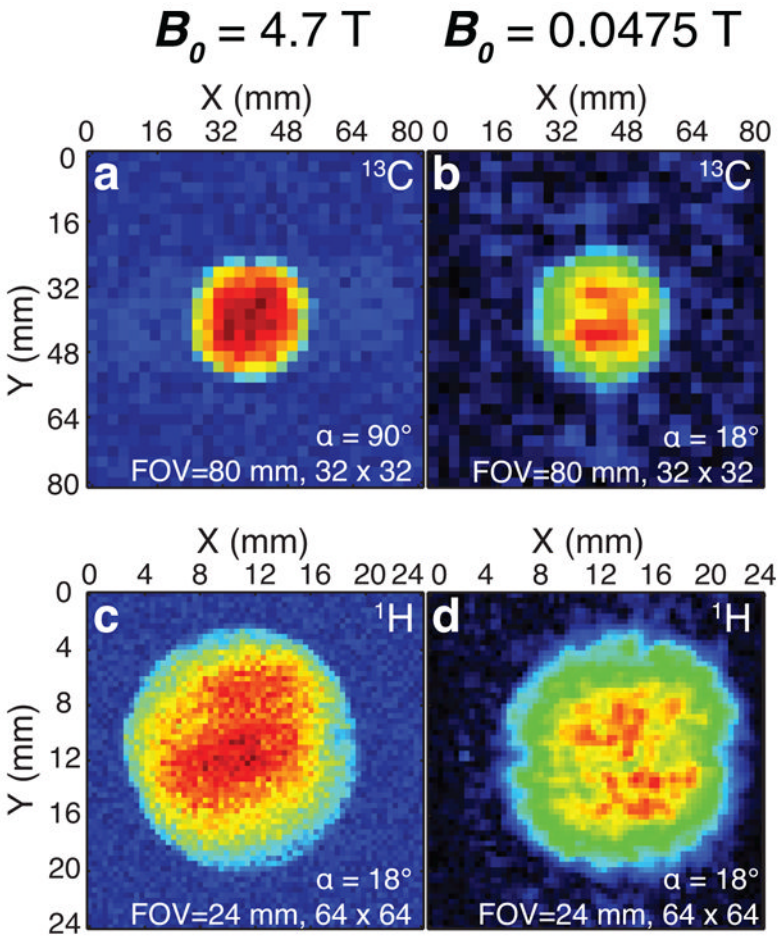

Fig 1.

^{13}C and ^{1}H MRI of sodium 1-^{13}C-acetate. 4.7 T acquisition used Boltzmann ^{13}C P = $4.06*10^{-6}$ and ^{1}H P = $1.61*10^{-5}$, and 0.0475 T used approximately the same polarization levels, ^{13}C P = $4.70*10^{-6}$ and ^{1}H P = $1.05*10^{-5}$. All measurements used a spherical phantom: for ^{1}H 1.0 g sodium 1-^{13}C-acetate in 99.8% D_2O with 2.8 mL total volume and for ^{13}C 5.18 g sodium 1-^{13}C-acetate in 99.8% D_2O with 17.5 mL total volume. All acquisition and processing parameters were identical except ^{13}C excitation pulse angle α. No image extrapolation or zero filling was used.

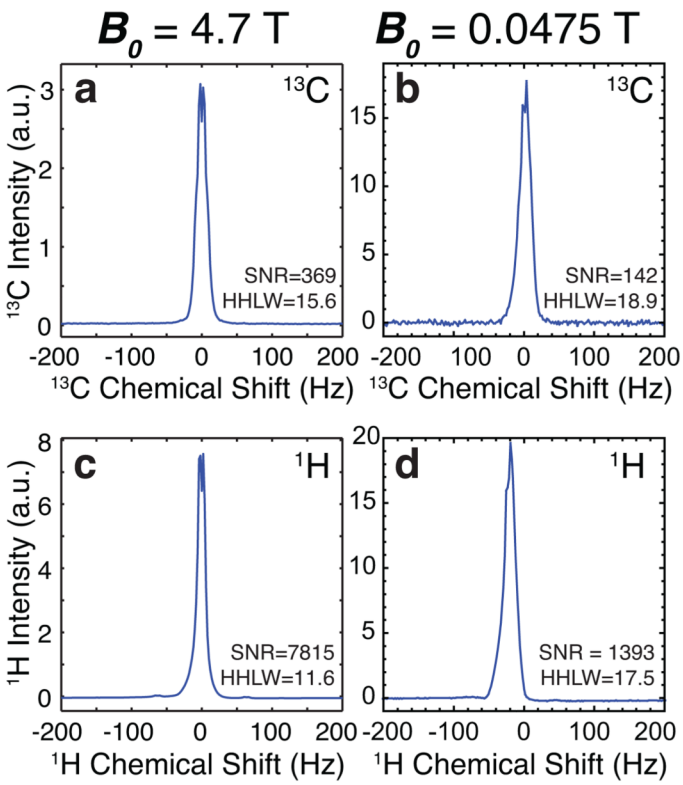

Fig 2.

^{13}C and ^{1}H NMR spectroscopy of sodium 1-^{13}C-acetate. 4.7 T acquisition used Boltzmann ^{13}C $P = 4.06*10^{-6}$ and ^{1}H $P = 1.61*10^{-5}$, and 0.0475 T used approximately the same polarization levels, ^{13}C $P = 4.70*10^{-6}$ and ^{1}H $P = 1.05*10^{-5}$. All measurements used a spherical phantom: for ^{1}H 1.0 g sodium 1-^{13}C-acetate in 99.8% D_2O with 2.8 mL total volume and for ^{13}C 5.18 g sodium 1-^{13}C-acetate in 99.8% D_2O with 17.5 mL total volume. All NMR acquisition and processing parameters were identical.

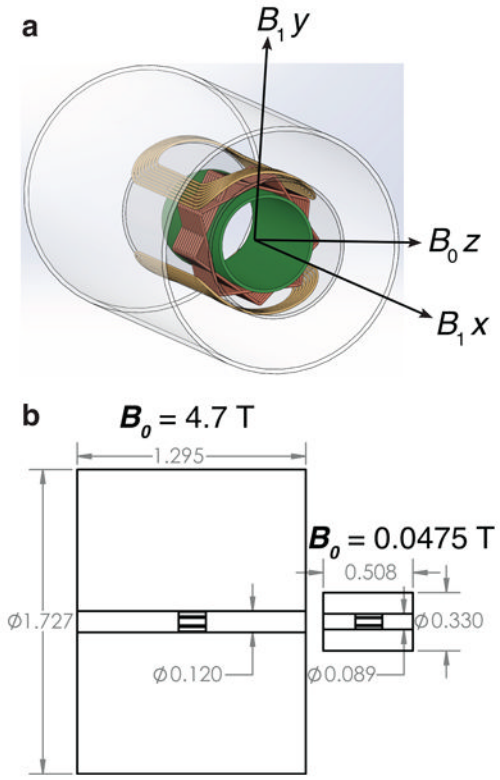

Fig 3.

MRI instrumentation. A) Schematic representation and alignment of the RF coils and shield to the B_0 magnet, and B) scale comparison of the 4.7 T and 0.0475 T MRI scanners. The dimensions provided are in meters.